Using foreshocks to constrain earthquake nucleation: low foreshock to aftershock ratios in the Hikurangi subduction zone

Authors:

Rebecca L Colquhoun [1] (rebeccalcolquhoun@gmail.com);

Jessica C. Hawthorne [1] (jessica.hawthorne@earth.ox.ac.uk)

[1]Department of Earth Sciences, University of Oxford, 3 South Parks Road, Oxford, OX1 3AN, United Kingdom

This manuscript is a preprint that has not undergone peer review. It has been submitted to the Earth and Planetary Science Letters. Subsequent versions of this manuscript may have different content. If accepted, the final peer-reviewed version will be linked from this webpage. Please feel free to contact any of the authors directly to comment on the manuscript.

Highlights

Using foreshocks to constrain earthquake nucleation: low foreshock to aftershock ratios in the Hikurangi subduction zone

Rebecca L. Colquhoun, Jessica C. Hawthorne

- We make new observations of foreshocks and aftershocks using phase coherence.
- Simple earthquake-earthquake triggering predicts foreshock and aftershock numbers.
- We detect fewer foreshocks than expected from this simple ETAS based model.
- This suggests that nucleation is more extended and complex.
- Therefore, external processes must be involved in earthquake nucleation.

Using foreshocks to constrain earthquake nucleation: low foreshock to aftershock ratios in the Hikurangi subduction zone

Rebecca L. Colquhoun[a], Jessica C. Hawthorne[a]

[a] *Department of Earth Sciences, University of Oxford, 3 South Parks Road, Oxford, OX1 3AN, United Kingdom*

Abstract

The complexity and duration of earthquake nucleation is an open question. Our understanding of this process is limited by a lack of high-quality observations of foreshocks and aftershocks. We therefore apply a coherence-based template matching approach to search for more foreshocks and aftershocks. We examine the half-hour before thousands of $M \geq 3$ mainshocks on the Hikurangi subduction zone in New Zealand, and make new detections of foreshocks and aftershocks which are close in space and time to the mainshocks. For $M \geq 4$ events, we find 68% fewer foreshocks than expected if earthquake nucleation is explained by the most intuitive type of earthquake-earthquake triggering: single-mode triggering. The number of foreshocks suggests that nucleation must be more extended and complex, perhaps driven by external processes like pore-pressure changes.

Keywords: Earthquake nucleation, Hikurangi subduction zone, ETAS, Phase coherence, Omori law, Foreshocks,

PACS: 91.30.pa

2000 MSC: 86A17

1. Introduction

There have been varied observations of foreshocks before earthquakes. For example, Trugman and Ross (2019) suggest that 72% of earthquakes in Southern California are preceded by increases in earthquake activity. Other authors find the foreshock rate to be around 40-55% (Jones and Molnar, 1976; Abercrombie and Mori, 1996; Chen and Shearer, 2016), and van den Ende and Ampuero (2020) find that as few as 18% of earthquakes in southern California have increases in seismicity which cannot simply be explained by variations in background seismicity rate. Significant foreshock activity is expected from rate and state models (Dieterich, 1994; Marone, 1998) and is observed on short time-scales in laboratory experiments (e.g Scholz, 1968; Johnson et al., 2013; Goebel et al., 2013; McLaskey and Kilgore, 2013; McLaskey and Lockner, 2014; Rouet-Leduc et al., 2017; Bolton et al., 2019, 2020; Dresen et al., 2020).

A number of researchers have investigated foreshocks because these events can provide insights into earthquake nucleation. On one hand, nucleation may be a complex, extended process that last minutes to months. Seismologists have observed significant increases in seismicity in the hours to days before large earthquakes in Southern California (Dodge et al., 1996; Chen and Shearer, 2016), in the North Pacific (Bouchon et al., 2013), in Kyushu, SW Japan (Kato et al., 2016), and on the East Pacific Rise (McGuire et al., 2005). Some statistical analyses suggest that these foreshocks, mainshocks, and aftershocks nucleate or are triggered via different processes (Brodsky, 2011; Shearer, 2012; Seif et al., 2018). Some of these processes could create complex, long-duration nucleation, as is sometimes inferred from observations. For instance, Tape et al. (2018) identified foreshock sequences before earthquakes in Alaska that lasted tens of seconds. These sequences may represent earthquake nucleation triggered by a propagating aseismic front. Similarly, Bouchon et al. (2011) identified an extended seismic signal before the 1999 İzmit earthquake. Complex, two-stage, nucleation has also been observed in laboratory studies (Latour et al., 2013; Harbord et al., 2017) and over very short durations at the beginning of earthquakes in California (Ellsworth and Beroza, 1995; Beroza and Ellsworth, 1996). Complex nucleation could last months, or occur intensely for minutes, and may result from aseismic nucleation processes (Dodge et al., 1996) or from the interaction of pore-fluid pressure changes on the accelerating fault Liu and Rice (2007).

However, other researchers have found that nucleation could be short and simple: that all clustering of earthquakes can be explained by earthquake-earthquake triggering (Helmstetter and Sornette, 2003b; Felzer et al., 2004; Yoon et al., 2019). For example, Felzer et al. (2004) were able to explain foreshock occurrences solely through the same earthquake-earthquake triggering which is responsible for aftershocks, and Ellsworth and Bulut (2018) suggest that no aseismic processes were involved in the foreshock sequence preceding the 1999 İzmit earthquake. Epidemic Type Aftershock Sequence models (ETAS, Ogata, 1988) often model foreshock and aftershock behaviour well, using relatively simple earthquake-earthquake triggering.

It has been difficult to understand the process of earthquake nucleation due to the limited availability of high-quality observations of foreshocks and aftershocks, particularly on short timescales. In this work, we seek to add one more observation of foreshock rates. We look for foreshocks, aftershocks, and sequences of foreshocks around thousands of earthquakes in New Zealand. We use a phase coherence-based technique to detect small events that are located spatially close to and within an hour-long window centred on each mainshock. We then compare the observed foreshock:aftershock ratio to the ratio expected from a particular case of earthquake-earthquake triggering: single-mode triggering.

1.1. Single-mode triggering

Single-mode triggering is a type of earthquake-earthquake triggering which requires that all clustering results from inter-earthquake triggering. It also maintains a type of self-similarity; the number of aftershocks scales via a power law relationship to the mainshock moment (e.g. Yamanaka and Shimazaki, 1990). The power law is chosen so that the average magnitude difference between a mainshock and its largest aftershock is independent of mainshock magnitude, following the empirical Båth's law (Båth, 1965; Felzer et al., 2002; Helmstetter and Sornette, 2003a; Felzer et al., 2004). Single-mode triggering can be viewed as a subset of ETAS models (Ogata, 1988).

2. Mainshock and data selection

We begin by identifying mainshocks to search around for foreshocks and aftershocks.

2.1. Seismic data and earthquake catalogue

We investigate earthquakes on the Hikurangi subduction zone beneath the North Island of New Zealand (Figure 1). The Hikurangi subduction zone is an ideal place to test whether external processes are involved in earthquake nucleation. The region hosts slow slip events as well as spatially variable pore fluid pressures

(Wallace et al., 2012; Naif and Key, 2018): two phenomena that could encourage extended earthquake nucleation.

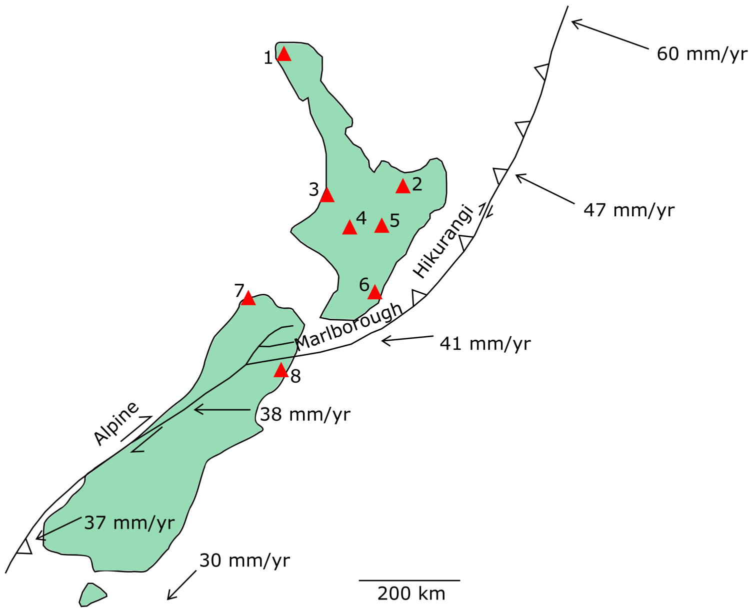

Figure 1: Map of New Zealand with major faults (lines), convergence rates (arrows) and stations (triangles) used. Convergence rates are in mm yr^{-1}, based on Wallace et al. (2012). Stations are all part of the GNS network (FDSN network code NZ) and are numbered as below:
1 – OUZ; 2 – URZ; 3 – HIZ; 4 – WPVZ; 5 – BKZ; 6 – BFZ; 7 – QRZ; 8 – KHZ

We use events listed in the GNS catalogue: the catalogue created by New Zealand's Te Pū Ao, or Institute of Geological and Nuclear Sciences. We gather seismograms from GNS seismic stations stored in the IRIS data center, using the obspyDMT software (Hosseini and Sigloch, 2017). Only stations within 4° of an earthquake's epicentre are included.

2.2. Identifying mainshocks

The initial earthquake catalogue consists of 12,769 M$\geq$ 3 events between 2005-01-01 and 2020-01-01, in a region between 175° and 180°W and 37° and 40°S, with no constraint on focal mechanism. Of these earthquakes, 11,236 have usable data: there is at least one station where all 3 components have data for an hour before and after these earthquakes.

Each of the identified M≥3 earthquakes is a candidate mainshock. However, even M≥3 earthquakes are clustered, and we want to consider our mainshock earthquakes independently, or in isolation. To be able to isolate mainshocks, we want the background seismicity to be constant throughout the 30 minutes before and after the earthquake being considered. But after an earthquake, the rate of seismicity is rapidly changing at first (aftershock decay), before becoming more steady, and so we do not want our mainshock to be too close in time to previous large earthquakes. Therefore we accept an earthquake to be a mainshock only if it is larger than all other earthquakes within a certain time interval and within a distance radius of 0.3°. All results presented consider the largest event within 24 hours (giving $n = 1365$), but we obtain similar results using other isolation windows (4–100 hours, table 1).

3. Methods

Once we have identified our mainshocks, we can search for foreshocks and aftershocks.

3.1. Mainshock templates

To begin, we identify and extract each mainshock's P waves to use as templates. We begin the template 1 second before the P-wave pick. We make a preliminary estimation of the P-wave pick by calculating the travel time of the earthquake waves to each station using obspy TauP (Crotwell et al., 1999) and the AK135 model (Kennett et al., 1995). This calculation predicts the P pick to within ±10 s. To improve the pick accuracy, we then apply a STA-LTA algorithm to a highpassed version of the data in this 20 second window, using a corner frequency of 1.5 Hz. The earliest STA-LTA trigger (Withers et al., 1998) on any component is taken as the P wave arrival. After we identify the arrival, we bandpass filter the data to between 1.5 and 10 Hz and extract an interval from 1 second before to 2 seconds after the P arrival pick. This part of the seismogram is our template.

3.2. Phase coherence calculation: Theory

We use this template to search for earthquakes with similar Green's functions. We search for earthquakes in a one-hour window of the continuous data, 30-minutes either side of the mainshock. We use the phase coherence method outlined by Hawthorne and Ampuero (2017), which identifies co-located seismic sources by comparing the seismograms recorded at multiple stations or components. Specifically, we calculate the phase coherence:

$$C_p = \mathrm{Re}\left[\frac{\hat{x}_k \hat{x}_l^*}{|\hat{x}_k \hat{x}_l^*|}\right] \approx \mathrm{Re}\left[\frac{\left(\hat{d}_{ck}\hat{d}_{tk}^*\right)\left(\hat{d}_{cl}\hat{d}_{tl}^*\right)^*}{\left|\left(\hat{d}_{ck}\hat{d}_{tk}^*\right)\left(\hat{d}_{cl}\hat{d}_{tl}^*\right)^*\right|}\right]. \tag{1}$$

In computing each term in parentheses (each $\hat{x}_k$ or $\hat{x}_l$), we are comparing the template and continuous data. $\hat{x}_k$ is the cross spectrum of the template signal (d_{tk}) and the continuous data (d_{ck}) at station or component k or l. Hats indicate Fourier transforms. Then when we compute the cross-spectrum of $\hat{x}_k$ and $\hat{x}_l$, we are looking for coherence between two stations or components k and l.

The C_p value should be high if the continuous data contains a source co-located with the template. In this case, the inter-source correlations implicit in the $\hat{x}_k = \hat{d}_{ck}\hat{d}_{tk}^*$ calculations turn out to eliminate the phases of the Green's function. The subsequent inter-station or inter-component correlations, implicit in the $\hat{x}_k - \hat{x}_l^*$ multiplications, eliminate the phases of the source time functions. So if the continuous data segment contains a source co-located with the template, all the phases which result from intersource cross-correlation (x_k and x_l) are eliminated. Both the numerator and denominator should be real and positive, and C_p should equal 1.

In other words, and perhaps more simply, if the continuous and template data are created by co-located earthquakes, their seismograms at station or component k can be written as $d_{ck} = s_c * g_k$ and $d_{tk} = s_t * g_k$. Here s_c and s_t are source time functions, and g_k is a common Green's function. In this case,

$$C_p = \mathrm{Re}\left[\frac{\left(\left(\hat{s}_c\hat{g}_k\right)\left(\hat{s}_t\hat{g}_k\right)^*\right)\left(\left(\hat{s}_c\hat{g}_l\right)\left(\hat{s}_t\hat{g}_l\right)^*\right)^*}{\left|\left(\left(\hat{s}_c\hat{g}_k\right)\left(\hat{s}_t\hat{g}_k\right)^*\right)\left(\left(\hat{s}_c\hat{g}_l\right)\left(\hat{s}_t\hat{g}_l\right)^*\right)^*\right|}\right] = 1. \tag{2}$$

In reality, of course, C_p never reaches 1 because equation 2 is not exact. The data are modified when windows of the seismograms are extracted for calculation. We therefore search for significantly positive values of C_p, and we follow the windowing and tapering approach used by Hawthorne and Ampuero (2017) to mitigate the effects of truncation. Specifically, we cross-correlate our templates with the continuous data without windowing over the entire continuous time series. We then extract 1 second windows of the data and calculate $\hat{x}$.

This phase coherence method allows us to search for a variety of signal types. It can identify nearby seismic sources even if they have complex, extended source time functions. We can detect foreshocks with source time functions similar to the mainshock, foreshocks with shorter source time functions, and any tremor-like foreshock sequences.

3.3. Results of the Phase Coherence calculation

We compute two types of phase coherence (Equation 1): C_{p-stat}, the inter-station phase coherence; and C_{p-comp}, the inter-component phase coherence. We calculate both in 1-second windows, separated by 0.2 s, for 1800 s before and after each mainshock and plot the results in Figure 2.

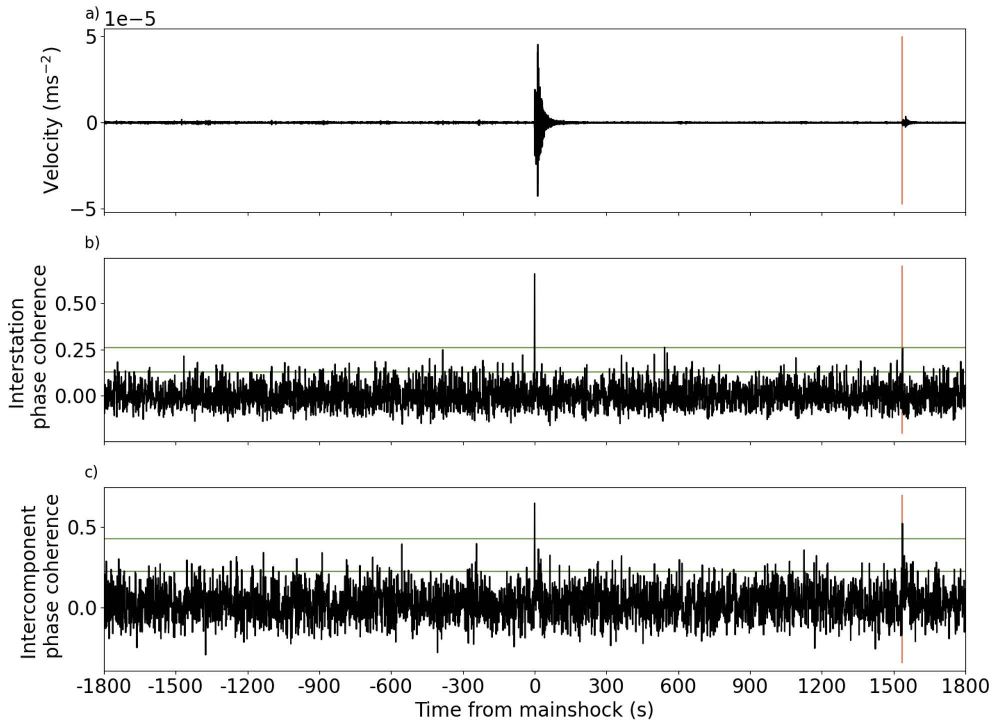

Figure 2: a): Velocity seismogram at one station (NZ.BFZ) for 1 hour around an earthquake (2019-10-19 at 17:28:31.26; 37.919°S, 176.426°E; 4.3 mb).
b): Inter-station phase coherence.
c): Inter-component phase coherence.
In b) and c), time is centered on the mainshock and horizontal lines denote 2 and 4 s.d. above the mean phase coherence values.

We cross-correlate the signal from different stations to find the inter-station coherence: k and l index different stations in equation 1. Inter-station coherence can only detect earthquakes which are within a fraction of a seismic wavelength of the mainshock (Geller and Mueller, 1980). Any shift in the earthquake location shifts the station arrival times. The time shifts make the Green's functions (g in equation 2) appear different between the mainshock and foreshock and thus reduce the phase coherence between the two signals.

Inter-component phase coherence quantifies coherence between the different components (E, N, Z) at the same station: k and l index different components in equation 1. The limited number of channels makes the output noisier. However, this approach also allows us to detect foreshocks and aftershocks that are some distance from the mainshock. With inter-component coherence, shifted earthquake locations still change the station arrival times, but the time shifts are the same across all three components at a given station, and those time-shifts are eliminated when we compute the inter-component coherence. C_{p-comp} thus measures the similarity in the shape of the Green's functions between the mainshock template and a window of the continuous signal (Gombert and Hawthorne, 2022).

We set thresholds to define detections within the continuous phase coherence records. We take the mean of the phase coherence over the full 3600 seconds. We define a detection as when the phase coherence exceeds 2, 3, or 4 times the standard deviation from the mean. We plot histograms of the number of detections in C_{p-stat} and C_{p-comp} through time in Figure 3.

To assess the uncertainty in the detection rate through time, we use bootstrap resampling to recompute the number of detections using different subsets of the mainshock population. To create each subset, we resample the mainshock population randomly, with replacement, until the resampled population is the same size as the original population. We then calculate the detection rate again. We

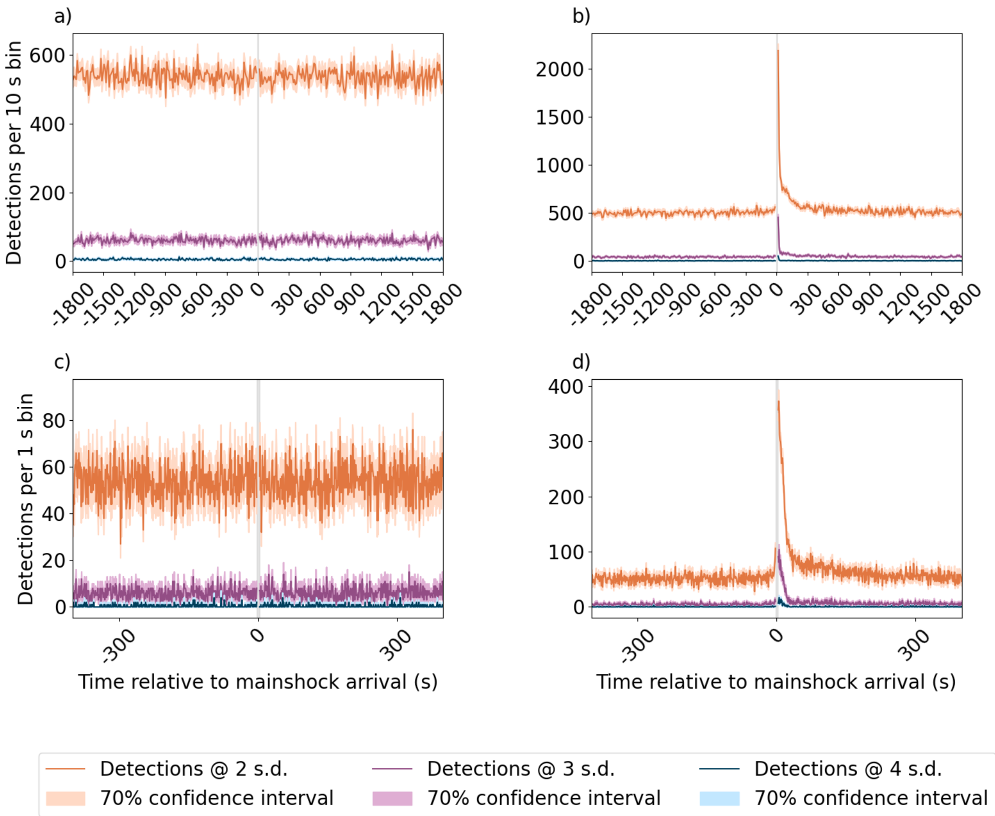

Figure 3: Plots of detections in phase coherence through time. The lines join the midpoint of the top of each histogram bar, showing the distribution in the number of detections through time. Panels a) and c) show interstation phase coherence whilst panels b) and d) show intercomponent phase coherence. Panels a) and b) show the full time around the earthquake and bin detections into 10 s bins. Panels c) and d) show 400s before and after the mainshock and use 1 s bins. Shading shows the 70% confidence interval. Orange line and shading is for detections at 2 s.d., purple for 3 s.d., and blue for 4 s.d.

repeat this process 100 times to estimate the uncertainty on the detection rate, as illustrated with the shading in Figure 3.

3.4. Magnitude resolution

We want to compare our detections to expectations from single-mode triggering. That comparison will require knowledge of our detection capability. Here, then, we estimate the magnitude of completeness of our detections.

We first subtract the background detection rate from our total number of detections. That leaves us with 11,233 combined foreshock and aftershock detections. All of our foreshocks and aftershocks are smaller than M3, as we considered all $M \geq 3$ earthquakes in the GNS catalogue as potential mainshocks. Some of our foreshocks and aftershocks are between M2.5 and 3. These earthquakes should be in the GNS catalogue, as that catalogue is complete to M2.5. So we search the GNS catalogue for $M2.5-3$ earthquakes that occur close to and at the same time as our detections. We identify 918 such earthquakes distributed at a range of times before and after the mainshocks. We again subtract the background rate and infer that 100 of our foreshock and aftershock detections are in the GNS catalogue with magnitudes between 2.5 and 3.

We use the number of M2.5–3 foreshocks and aftershocks ($N_{2.5>M>3}$) to find the parameter a of a Gutenberg-Richter distribution ($N_{M>M_{\mathrm{ref}}} = 10^{a-bM_{\mathrm{ref}}}$). Here a is a measure of the total seismicity in the region, and we estimate it to be 4.665 We take $b = 1$, as estimated in section 5) to constrain the relative numbers of large and small earthquakes.

Then we can calculate the number of events above any given minimum magnitude M_{min}:

$$N(M > M_{min}) = 10^a(10^{-M_{min}}), \tag{3}$$

We set this number equal to 11,233, the number of foreshocks and aftershocks we detect, and solve for the minimum magnitude M_{min}, obtaining

$$M_{min} = -\log_{10}\left(\frac{11233}{10^{4.665}}\right) = 0.61. \tag{4}$$

These calculations suggest that we have detected earthquakes down to around $M0.6$.

4. Patterns in phase coherence through time

Now that we have numerous earthquake detections and an estimate of the range of earthquake magnitudes, we examine how the number of detections varies with time from the mainshock. Throughout our calculations, we ignore detections between -1 s and 2 s of the mainshock, as that interval is contaminated by the mainshock.

If single-mode triggering controls all earthquake clustering, we expect the foreshock and aftershock rate to follow Omori's law, with the earthquake rate decaying as t^{-1} with time before or after the mainshock (Parsons, 2002; Helmstetter et al., 2003; Felzer et al., 2004). However, if nucleation is more complex, and external processes influence slip acceleration, the earthquake rate may or may not follow this characteristic power-law decay.

4.1. Inter-station Coherence

Figure 3a shows the inter-station detections through time, averaged across all three components. We do not see any patterns in the detection rate. The detection rate is constant within error, with a rate of 544 detections per 10-second bin, outside of the window around the mainshock. We also see no variation in detection rate on a shorter timescale: in the 400 s before and after the mainshock, using a histogram bin width of 1 s (Figure 3c).

4.2. Inter-component

Inter-component phase coherence, averaged across different stations has a background detection rate of about 495 per 10-s time bin (Figure 3b). Many of these are false detections, where noise in the 3-component calculation happens to be slightly coherent with the template, but that false detection rate is constant in time. On top of the constant, we see a variation in detection rate which appears to come from foreshocks and aftershocks. The number of detections increases just before the mainshock and then gradually decreases after the mainshock. Even after the detection rate has decreased and starts to level out, the number of detections remains slightly elevated; we consider only 30 minutes after the mainshock, and seismicity has not yet returned to regular background levels.

Shorter-timescale variations may be better seen in Figure 3d, where we plot the detection rate in the 400 s before and after the mainshock, using 1-s bins. The detection rate increases abruptly in the seconds before the mainshock. After the mainshock, detections decrease steadily following a power-law distribution.

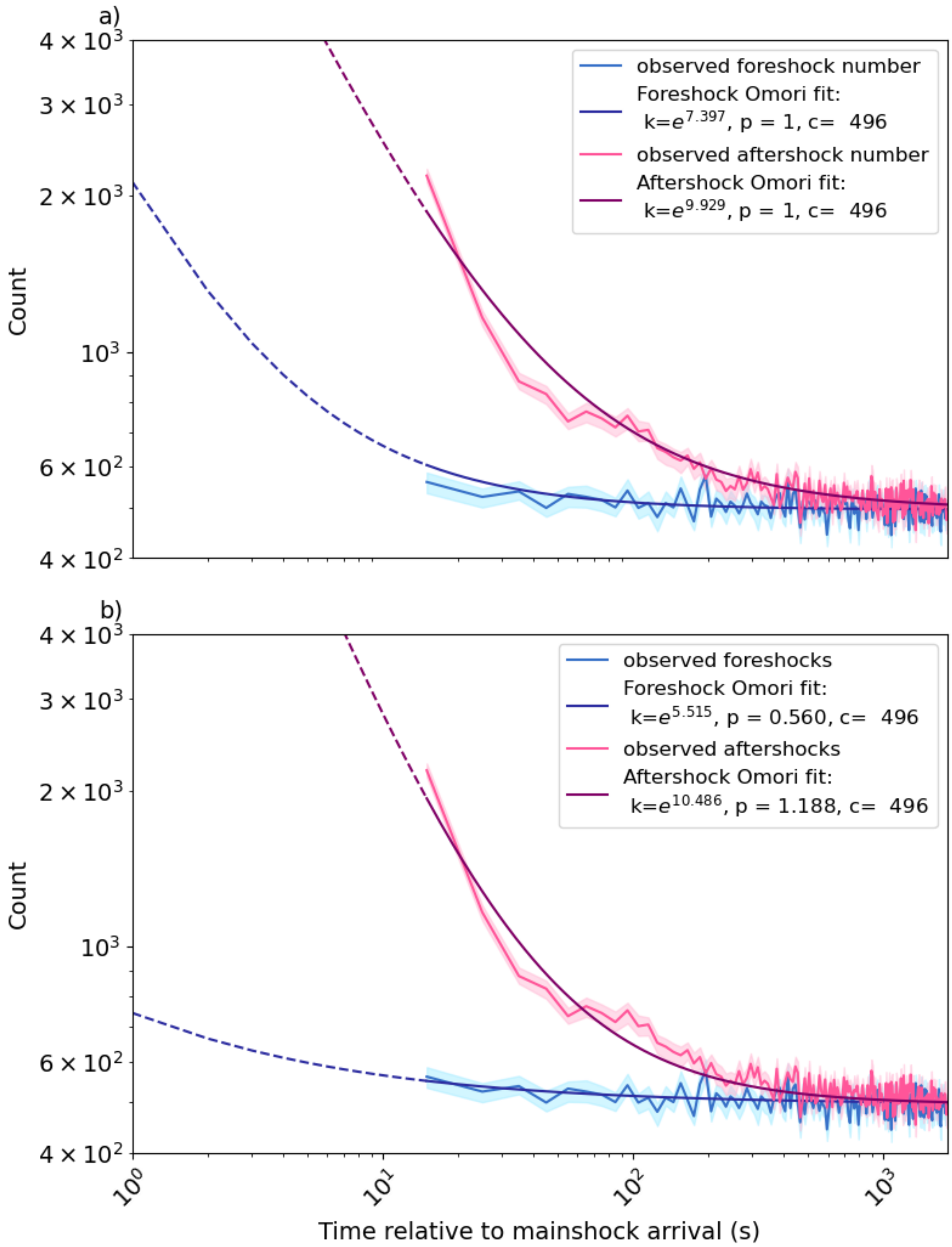

Figure 4: Log-log plots of foreshock (blue) and aftershock (pink) detections at two standard deviations time relative to mainshock arrival. Power law relations, following Omori's law, are plotted: in a) with the p-exponent fixed to 1, and in b) where p is optimised independently for foreshocks and aftershocks. The asymptote for both is fixed at the background detection value over the first 500 s (496 detections/10 s bin). The point at 5 s (corresponding to 0-10 s for aftershocks and -10 –0 s for the foreshocks) is not plotted, as we remove all detections within $\pm$2s of the mainshock due the peak spreading.

4.3. Temporal patterns in foreshock and aftershock activity

To better examine the distribution in time of our detections, we plot them in log-log space, where we see a clear power-law decay in detections (Figure 4a). In single-mode triggering, the seismicity rate before or after a mainshock decays as time^{-p}, following Omori's law (Utsu et al., 1995). Here p is a decay parameter which is typically around 1. If foreshocks and aftershocks both result from inter-earthquake triggering, we expect the same p value to describe both Omori fits.

Here we attempt to fit our foreshock and aftershock rate as

$$N(t) = C_1 + C_2 t^{-p}, \tag{5}$$

where C_1 is a constant representing the background rate, including false detections, and C_2 is a constant representing the number of foreshocks or aftershocks. The aftershock distribution is fit well by this Omori's law scaling, using $p = 1$. Figure 4a shows that the observed aftershock rate, denoted by the pink curve (shading showing 70% confidence interval), is close to the best-fit Omori curve (purple curve) at all times from the mainshock. In fitting the Omori law curve, we fix C_1 as the background seismicity rate, calculated over the first 500 seconds, and look to optimise C_2.

In figure 4b, we optimise for the exponent, p, as well as for C_2. Whilst the Omori law with $p = 1$ gives a reasonable fit by eye, the optimised value of $p = 0.56$ shows that a better fit is achieved by varying the p value away from 1.

5. Foreshock:aftershock ratio

Next, however, we consider a more rigorous assessment of a single-mode triggering model. We compare the observed foreshock:aftershock ratio to that expected from single-mode triggering.

5.1. Observations

To compute the number of foreshocks and aftershocks, we first subtract the background detection rate: the average rate in the -1800 to -1400 seconds before the mainshock. We assume that each remaining detection represents a single earthquake, and we sum the number of detections before and after the mainshocks to get the number of foreshocks and aftershocks, respectively. We then compute the foreshock:aftershock ratio for groups of mainshocks with different magnitudes.

In Figure 5, we plot the observed ratio (navy line) and its bootstrapped distribution and confidence intervals (blue bars). Figure 6 better allows us to compare between the different magnitude groups. We see the ratio increase as smaller magnitudes are considered.

		Declustering window (hours)							
		4	8	12	24	36	48	72	100
Background Window (seconds)	100	0.0475	0.0507	0.0490	0.0350	0.0606	0.0619	-0.0176	0.0509
	200	0.0741	0.0720	0.0606	0.0489	0.0473	0.0644	0.0110	0.0494
	400	0.0707	0.0813	0.0844	0.0903	0.0922	0.0929	0.0524	0.0867
	600	0.0424	0.0405	0.0411	0.0451	0.0411	0.0449	0.0197	0.0207
	800	0.0568	0.0563	0.0588	0.0635	0.0626	0.0610	0.0480	0.0509
	1000	0.0395	0.0361	0.0349	0.0381	0.0336	0.0284	0.0283	0.0318

Table 1: Foreshock:aftershock ratios for M4+ events using different background windows for calculating background seismicity and declustering events at different windows.

The declustering window and background window have some effect on the foreshock:aftershock ratio we find. However, the variation of the ratio is within

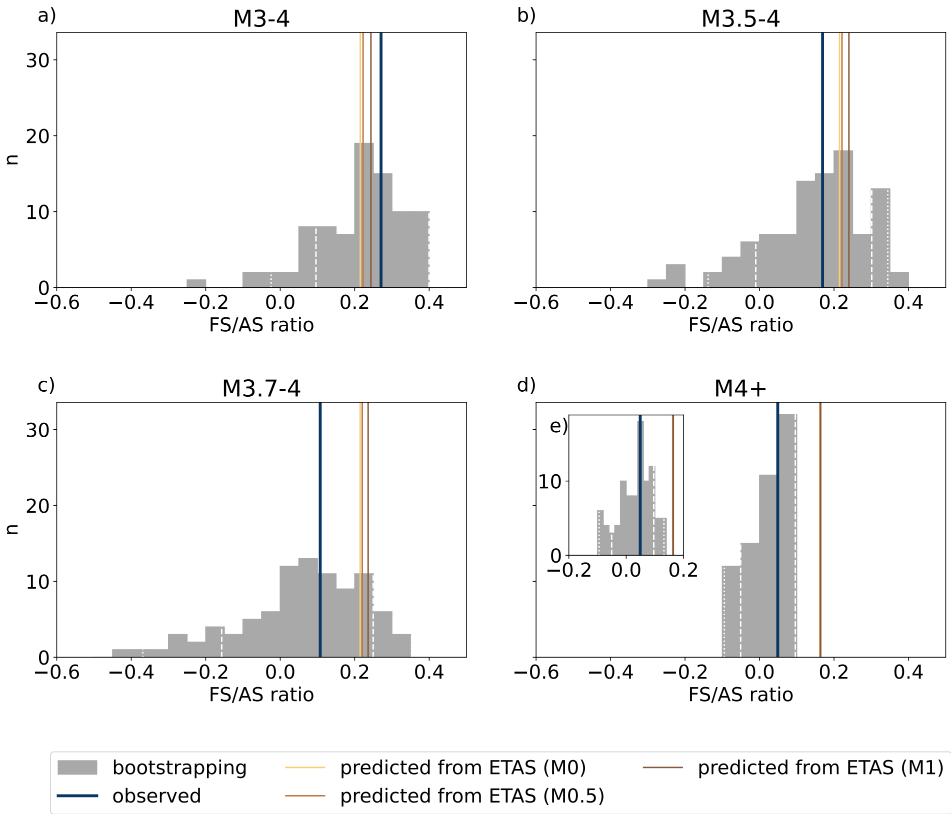

Figure 5: Histograms of the bootstrapping of the foreshock:aftershock ratio calculation (grey). Panels include events from different magnitude groupings: a) M3–4, b) M3.5-4, c) M3.7–4, and d) M4+. Inset panel e) looks at M4+ events with a bin size of 0.02. The dark blue line shows the calculated ratio. White dashed lines denote the 70% confidence interval, and white dotted lines the 90% confidence interval, found from bootstrapping. Brown lines indicate ratio expected from ETAS with detection limits of M0 (lightest), 0.5 (medium), and 1 (darkest).

the uncertainty we find through bootstrapping (Table 1).

5.2. Predictions from single-mode triggering

In an ETAS model, the number of aftershocks triggered by an earthquake of magnitude M is given by

$$N(t) = \frac{K}{(t+c)^P} = \frac{C\ 10^{\alpha(M-M_{min})}}{(t+c)^P}, \tag{6}$$

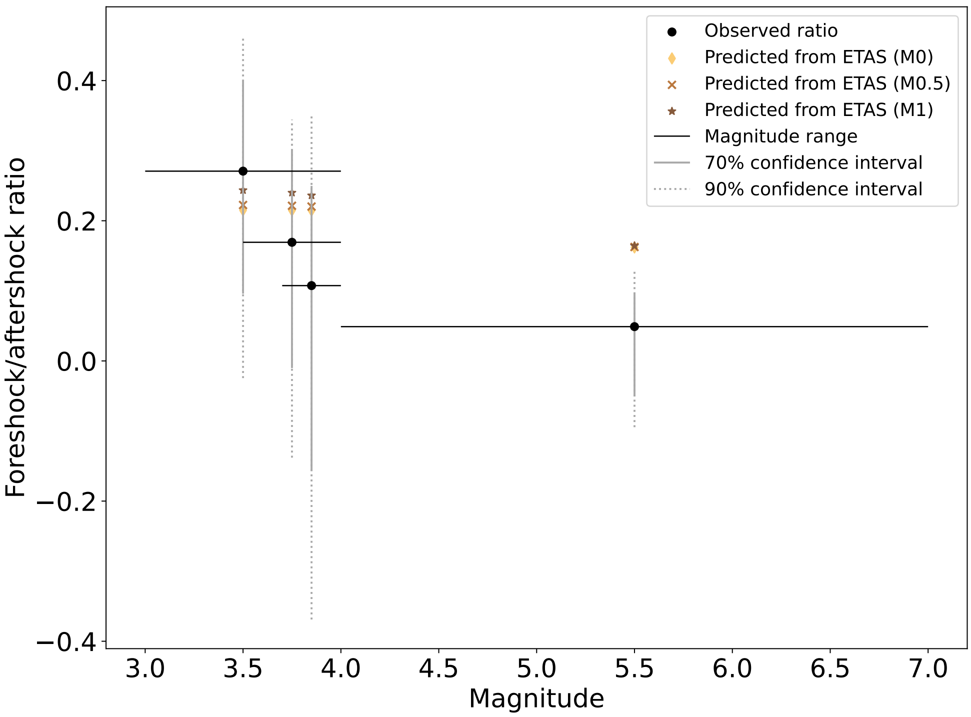

Figure 6: Comparison of the expected and observed foreshock-aftershock ratio for different mainshock magnitude groups (M3-4, M3.5-4, M3.7-4 and M4+). Horizontal black lines show the magnitude range considered, and symbols are at the midpoint of this range. Black dots show the observed ratio for each magnitude interval. Vertical grey lines show the confidence intervals: solid for the 70% confidence interval and dotted for the 90% confidence interval. Brown symbols indicate ratio expected from ETAS with detection limits of M0 (lightest, diamonds), 0.5 (medium, crosses) and 1 (darkest, stars). For M4+ events, the predicted values lie outside of the 90% confidence range of the observed value.

where K, C, and c are constants (Utsu et al., 1995), and M_{min} is the minimum magnitude we can detect.

We estimate the constants μ, K, α, c, p, and β by analysing the the GNS earthquake catalog, using BayesianETAS r package (Ross, 2021). We now apply this theory to calculate the foreshock to aftershock ratio expected for the GNS catalogue of mainshocks. We find that $\beta = 2.24$, which implies that the Gutenberg-Richter parameter $b = 0.97 \approx 1$. We find that $\mu = 2.54 \times 10^{-5}$, $K = 0.5$, $\alpha = 0.5$, and $c = 1.2$. We also calculate the branching ratio (r in Shearer, 2012), which can be interpreted as the proportion of the catalogue which is an aftershock (Helmstetter et al., 2003; Helmstetter and Sornette, 2003c).

We then use these parameters to calculate the expected numbers of foreshocks and aftershocks expected for each earthquake in our mainshock catalogue in the time window of interest, using the approach outlined by Shearer (2012) (Appendix B).

Finally, we sum the expected foreshock and aftershock numbers over subsets of the mainshocks. We consider the same subsets we considered in our observations: all the mainshocks (M3+), M3–4, M3.5–4, M3.7–4 and M4+.

The smallest magnitude of event we can detect is a major source of uncertainty. We estimated it to be ≈ 0.5 in Section 3.4, but we additionally do these calculations for detection limits of both $M0$ and $M1$.

5.3. Comparing observations and predictions

We also plot the expected foreshock:aftershock ratios for a detection completeness of M0, 0.5 and 1 alongside the observations in Figures 5 and 6, For M4+ events, the predicted ratios are lower than the detected ratio; we find a foreshock:aftershock ratio of 0.051, but single-mode ETAS predicts a ratio of 0.16. However, as we consider smaller mainshocks, the expected and observed ratios converge, and the difference between the predicted and observed ratio becomes insignificant (Figures 5 and 6).

5.4. Depth Dependence

The foreshock:aftershock ratio remains low for large-magnitude mainshocks even if we subdivide the catalogue into deep ($>$ 70km) and shallow events. The foreshock:aftershock ratio is 0.047 for shallow M$\geq$ 4 mainshocks and 0.020 for deep M$\geq$ 4 mainshocks. As in previous work, we find that deeper earthquakes have fewer foreshocks and aftershocks (Frohlich, 1987; Abercrombie and Mori, 1996; Chen and Shearer, 2016); shallow events ($<$ 70 km) comprise 58% of the mainshocks but 81% of the total foreshock detections (663) and 66% of the total aftershock detections (11434).

6. Sequences

The low foreshock:aftershock ratio suggests that earthquake nucleation is not entirely explained by single-mode triggering, but it is a relatively subtle indication. We therefore look for something which would more obviously indicate slip acceleration: foreshock sequences. For instance, Tape et al. (2018) identified intense, minute-long sequences of foreshocks before mainshocks in Alaska. We thus systematically look for sequences of detections before and after our mainshocks.

We look for sequences in windows of different lengths, from 5 to 20 s. For each window length, we compute the fraction of the 1-s bins which contain detections. We then compare this fraction to a range of thresholds, between 10% and 100%, to determine if the window contains a sequence. With these thresholds, we identify a large number of sequences, particularly at times close to the mainshock and for short window lengths (Figure 7).

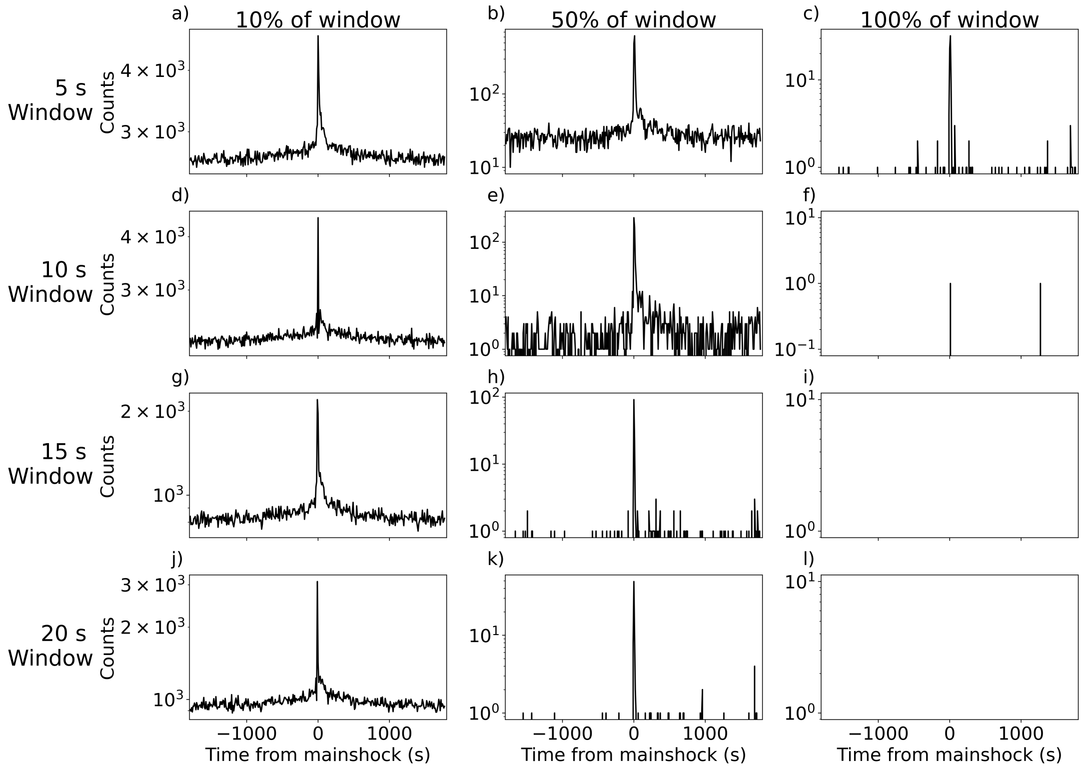

Figure 7: Histograms of detections of sequences for different time windows and proportion of window filled. The mainshock occurs at time 0, but to avoid any double counting, we ignore detections for the 2 seconds before and after it. Blank boxes show no sequences were detected.

We examine a number of the apparent sequences visually. In Figure 8, we show the phase coherence record and a seismogram for one of these sequences, shown by the blue box. This sequence has a detection in 4 out of the 5 seconds (80% of the window): the signal that originates in this time window is coherent with that of the mainshock. However, the signal appears to be small. It is not readily identifiable by eye.

We compare the ratio of sequences to detections in different time windows to

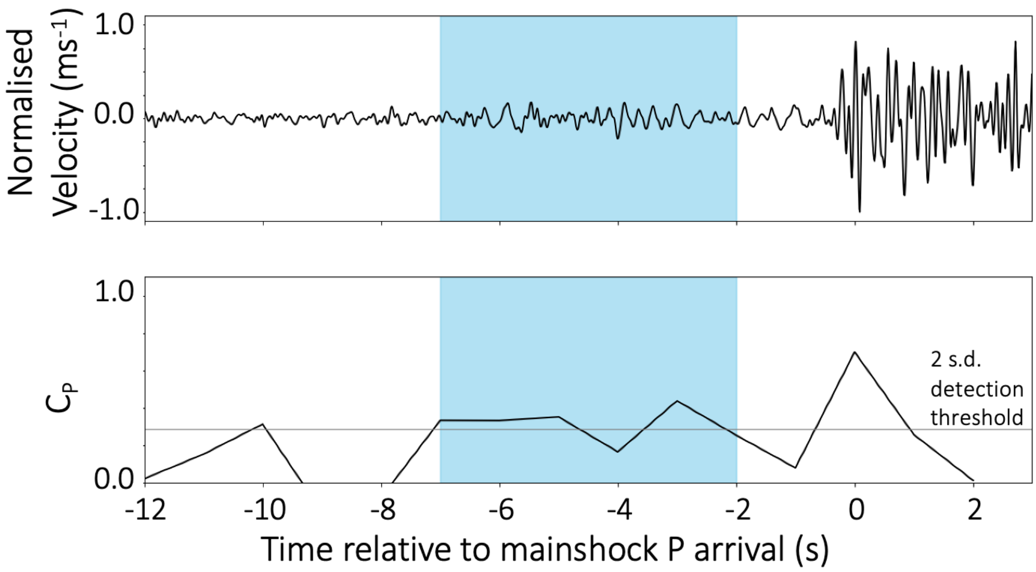

Figure 8: A sequence detection. The top panel shows a normalised velocity seismogram with the detected sequence highlighted by the blue box. The bottom panel shows the phase coherence value, with the horizontal grey line being 2 s.d. above the mean value. Note that the C_P value for much of this window is close to or above the detection limit. For comparison, the average C_p value of the full 3600 s record shown in figure 2 is 0.001.

see if there is a statistically significant increase in the number of sequences as we approach the mainshock.

Over the first 200 seconds of the record (-1800 – -1600 s, considered to be representative of the background), there are 0.0083 sequences per detection (considering a sequence to be 60%+ of a 5 second window). The 95% confidence interval on this number is 0.0075 – 0.0090. In the window 1750–1797 (the 50 seconds before the mainshock, removing the blanked window around the mainshock), the ratio is 0.0113. In other words the sequence rate has increased by 17% percent whilst the detection rate (including false detections) has increased by 10% percent. The more dramatic increase in sequence rate suggests the increased sequence rate comes from detection clustering, not just an increased number of detections though we have not robustly analysed the statistics.

As we consider larger proportions of the window, and longer windows, the sequence rate appears constant through time, but this may just result from an increase in the uncertainty, as very few sequences are identified in any one time interval.

7. Discussion

In this work, we have used a coherence-based approach to detect numerous foreshocks and aftershocks in the 30 minutes before and after mainshocks. The inter-station phase coherence, on the other hand, detects few to no foreshocks and aftershocks. The lack of inter-station detections could imply that 1) the foreshocks and aftershocks are not perfectly co-located with the mainshock or 2) the foreshocks and aftershocks are too small to be detected on more than one station.

We have chosen to analyse the detections made with inter-component phase coherence We find that:

1. Most robustly, the foreshock:aftershock ratio for M4+ mainshocks is lower than expected from single-mode ETAS.
2. For smaller (M3-4) mainshocks, the foreshock:aftershock ratio is similar to that expected from single-mode ETAS.
3. The foreshock rate is better fit by an Omori power law decay with $p = 0.56$, than one with $p = 1$.
4. There is a statistically significant increase in the number of foreshock sequences before the mainshocks, but there are no obvious tremor-like precursors.

We are not the first to conclude that the foreshock:aftershock ratio differs from that expected from single-mode triggering (Felzer et al., 2004). Shearer (2012) also found differing foreshock:aftershock ratios, though they found higher-than-expected foreshock:aftershock ratio, while we find a lower-than-expected ratio.

The low foreshock:aftershock ratio could in principle result from a detection bias. Aftershocks could occur closer to the mainshock than foreshocks, so that they are easier to detect. However, previous work found similar spatial distributions of foreshocks and aftershocks (Richards-Dinger et al., 2010; Brodsky, 2011), and it the aftershocks, not the foreshocks, that occur partially in the mainshock coda; which would make early aftershocks harder to detect (Peng et al., 2007; Lengliné et al., 2012).

It thus seems more likely that there is some physical cause of the low foreshock:aftershock ratio. The low ratio could arise if the fault conditions change between foreshocks and aftershocks (unlike Brodsky, 2011), so that earthquake-earthquake triggering occurs in different conditions (e.g. Helmstetter et al., 2003). This might also explain why the optimised value of the p exponent for foreshocks is 0.56 (aftershocks $p = 1.188$, figure 4b), rather than 1.

Several processes could reduce the foreshock rates prior to earthquakes or alter the conditions that earthquake-earthquake triggering occurs in.

For example, one could imagine that the pore pressure on the fault is high prior to larger ($M \geq 4$) earthquakes. Higher pore-pressure on the fault increases the minimum nucleation size and thus could reduce the potential for small-magnitude foreshocks (Ohnaka, 2000; Harbord et al., 2017). Alternatively, the fault zones that host $M > 4$ mainshocks could just require large amounts of slip for stress to evolve and thus have a large fracture energy. Such a large resistance to slip would favour large ruptures; it could make it harder for small foreshocks to occur (Keilis-Borok, 1957; Ohnaka, 2000; Rubin and Ampuero, 2005; Harbord et al., 2017; Cattania and Segall, 2019).

On the other hand, it is also possible that earthquakes are triggered not by each other but by an accelerating aseismic slip front (e.g., Bouchon et al., 2011; Ando et al., 2012; Tape et al., 2018). However, it is not obvious why aseismic slip would cause a low foreshock:aftershock ratio.

8. Conclusions

The nature of earthquake nucleation remains unclear. It is difficult to constrain the processes involved, be they simple or complex, because there are limited high-quality observations of foreshocks and aftershocks. Here we have made new observations of foreshocks and aftershocks around $M \geq 3$ mainshocks on the Hikurangi subduction zone. We used a template-based coherence approach to detect these small earthquakes.

We have found that the foreshock:aftershock ratio of $M \geq 4$ events is lower than that expected if earthquakes interact exclusively by single-mode triggering. Further, the temporal distribution of foreshocks is fit better by Omori's law with $p = 0.56$ than by $p = 1$. These observations suggest that an external process is involved in earthquake nucleation, perhaps changing the fault properties before and after the mainshock.

9. Acknowledgements

Rebecca Colquhoun is supported by a Natural Environment Research Council (NERC) Grant [NE/S007474/1] and an Oxford-Radcliffe Scholarship.

10. Data Acknowledgements

Processing was primarily in Python 3.7 and was undertaken using Scipy (Virtanen et al., 2020), Numpy (Harris et al., 2020), and Obspy (Beyreuther et al., 2010). Plotting used Matplotlib (Hunter, 2007). Data was downloaded using obspyDMT (Hosseini and Sigloch, 2017) and collected on the New Zealand seismic network, NZ. Code is available here: `https://github.com/RebeccaColquhoun/Colquhoun_and_Hawthorne_earthquake_precursors` and data was downloaded from the IRIS data repository.

References

Abercrombie, R.E., Mori, J., 1996. Occurrence patterns of foreshocks to large earthquakes in the western United States. Nature 381, 303–307. URL: https://www.nature.com/articles/381303a0, doi:10.1038/381303a0. number: 6580 Publisher: Nature Publishing Group.

Ando, R., Takeda, N., Yamashita, T., 2012. Propagation dynamics of seismic and aseismic slip governed by fault heterogeneity and Newtonian rheology. Journal of Geophysical Research: Solid Earth 117, n/a–n/a. URL: http://doi.wiley.com/10.1029/2012JB009532, doi:10.1029/2012JB009532.

Beroza, G.C., Ellsworth, W.L., 1996. Properties of the seismic nucleation phase. Tectonophysics 261, 209–227. doi:https://doi.org/10.1016/0040-1951(96)00067-4.

Beyreuther, M., Barsch, R., Krischer, L., Megies, T., Behr, Y., Wassermann, J., 2010. ObsPy: A Python Toolbox for Seismology. Seismological Research Letters 81, 530–533. URL: https://pubs.geoscienceworld.org/srl/article/81/3/530-533/143693, doi:10.1785/gssrl.81.3.530. tex.ids= beyreuther2010.

Bolton, D.C., Shokouhi, P., Rouet-Leduc, B., Hulbert, C., Rivière, J., Marone, C., Johnson, P.A., 2019. Characterizing Acoustic Signals and Searching for Precursors during the Laboratory Seismic Cycle Using Unsupervised Machine Learning. Seismological Research Letters 90, 1088–1098. URL: https://doi.org/10.1785/0220180367, doi:10.1785/0220180367.

Bolton, D.C., Shreedharan, S., Rivière, J., Marone, C., 2020. Acoustic Energy Release During the Laboratory Seismic Cycle: Insights on Laboratory Earthquake Precursors and Prediction. Journal of Geophysical Research: Solid Earth 125, e2019JB018975. URL: https://onlinelibrary.wiley.com/doi/abs/10.1029/2019JB018975, doi:10.1029/2019JB018975. _eprint: https://onlinelibrary.wiley.com/doi/pdf/10.1029/2019JB018975.

Bouchon, M., Durand, V., Marsan, D., Karabulut, H., Schmittbuhl, J., 2013. The long precursory phase of most large interplate earthquakes. Nature Geoscience 6, 299–302. URL: http://www.nature.com/articles/ngeo1770, doi:10.1038/ngeo1770. publisher: Nature Publishing Group.

Bouchon, M., Karabulut, H., Aktar, M., Özalaybey, S., Schmittbuhl, J., Bouin, M.P., 2011. Extended nucleation of the 1999 Mw7.6 Izmit earthquake. Science 331, 877–880. doi:10.1126/science.1197341.

Brodsky, E.E., 2011. The spatial density of foreshocks. Geophysical Research Letters 38. URL: http://doi.wiley.com/10.1029/2011GL047253, doi:10.1029/2011GL047253. publisher: John Wiley & Sons, Ltd.

Båth, M., 1965. Lateral inhomogeneities of the upper mantle. Tectonophysics 2, 483–

514. URL: https://linkinghub.elsevier.com/retrieve/pii/004019516590003X, doi:10.1016/0040-1951(65)90003-X.

Cattania, C., Segall, P., 2019. Crack Models of Repeating Earthquakes Predict Observed Moment-Recurrence Scaling. Journal of Geophysical Research: Solid Earth 124, 476–503. URL: https://onlinelibrary.wiley.com/doi/10.1029/2018JB016056, doi:10.1029/2018JB016056.

Chen, X., Shearer, P.M., 2016. Analysis of Foreshock Sequences in California and Implications for Earthquake Triggering. Pure and Applied Geophysics 173, 133–152. URL: https://doi.org/10.1007/s00024-015-1103-0, doi:10.1007/s00024-015-1103-0.

Crotwell, H.P., Owens, T.J., Ritsema, J., 1999. The TauP Toolkit: Flexible Seismic Travel-time and Ray-path Utilities. Seismological Research Letters 70, 154–160. URL: https://pubs.geoscienceworld.org/srl/article/70/2/154-160/142385, doi:10.1785/gssrl.70.2.154.

Dieterich, J., 1994. A constitutive law for rate of earthquake production and its application to earthquake clustering. Journal of Geophysical Research: Solid Earth 99, 2601–2618. URL: https://onlinelibrary.wiley.com/doi/abs/10.1029/93JB02581, doi:10.1029/93JB02581. _eprint: https://onlinelibrary.wiley.com/doi/pdf/10.1029/93JB02581.

Dodge, D.A., Beroza, G.C., Ellsworth, W.L., 1996. Detailed observations of California foreshock sequences: Implications for the earthquake initiation process. Journal of Geophysical Research: Solid Earth 101, 22371–22392. doi:10.1029/96jb02269.

Dresen, G., Kwiatek, G., Goebel, T., Ben-Zion, Y., 2020. Seismic and Aseismic Preparatory Processes Before Large Stick–Slip Failure. Pure and Applied Geophysics 177, 5741–5760. URL: https://doi.org/10.1007/s00024-020-02605-x, doi:10.1007/s00024-020-02605-x.

Ellsworth, W.L., Beroza, G.C., 1995. Seismic evidence for an earthquake nucleation phase. Science 268, 851–855. doi:10.1126/science.268.5212.851.

Ellsworth, W.L., Bulut, F., 2018. Nucleation of the 1999 Izmit earthquake by a triggered cascade of foreshocks. Nature Geoscience 11, 531–535. URL: http://dx.doi.org/10.1038/s41561-018-0145-1, doi:10.1038/s41561-018-0145-1. publisher: Springer US.

van den Ende, M.P.A., Ampuero, J.P., 2020. On the Statistical Significance of Foreshock Sequences in Southern California. Geophysical Research Letters 47, e2019GL086224.

URL: https://onlinelibrary.wiley.com/doi/abs/10.1029/2019GL086224, doi:10.1029/2019GL086224. _eprint: https://onlinelibrary.wiley.com/doi/pdf/10.1029/2019GL086224.

Felzer, K.R., Abercrombie, R.E., Ekström, G., 2004. A Common Origin for Aftershocks, Foreshocks, and Multiplets. Bulletin of the Seismological Society of America 94, 88–98. Tex.ids= felzer2004.

Felzer, K.R., Becker, T.W., Abercrombie, R.E., Ekström, G., Rice, J.R., 2002. Triggering of the 1999 M_w 7.1 Hector Mine earthquake by aftershocks of the 1992 M_w 7.3 Landers earthquake. Journal of Geophysical Research: Solid Earth 107, ESE 6–1–ESE 6–13. URL: http://doi.wiley.com/10.1029/2001JB000911, doi:10.1029/2001JB000911.

Frohlich, C., 1987. Aftershocks and temporal clustering of deep earthquakes. Journal of Geophysical Research: Solid Earth 92, 13944–13956. doi:10.1029/jb092ib13p13944.

Geller, R., Mueller, C., 1980. Four similar earthquakes in central California. Geophysical Research Letters 7, 821–824.

Goebel, T.H.W., Schorlemmer, D., Becker, T.W., Dresen, G., Sammis, C.G., 2013. Acoustic emissions document stress changes over many seismic cycles in stick-slip experiments. Geophysical Research Letters 40, 2049–2054. URL: https://onlinelibrary.wiley.com/doi/abs/10.1002/grl.50507, doi:10.1002/grl.50507. _eprint: https://onlinelibrary.wiley.com/doi/pdf/10.1002/grl.50507.

Gombert, B., Hawthorne, J., 2022. Rapid tremor migration during few minute-long slow earthquakes in Cascadia. preprint. Earth ArXiv. doi:10.31223/X56623.

Harbord, C.W., Nielsen, S.B., De Paola, N., Holdsworth, R.E., 2017. Earthquake nucleation on rough faults. Geology 45, 931–934. URL: http://pubs.geoscienceworld.org/geology/article/45/10/931/353550/Earthquake-nucleation-on-rough-faults, doi:10.1130/G39181.1. publisher: GeoScienceWorld.

Harris, C.R., Millman, K.J., van der Walt, S.J., Gommers, R., Virtanen, P., Cournapeau, D., Wieser, E., Taylor, J., Berg, S., Smith, N.J., Kern, R., Picus, M., Hoyer, S., van Kerkwijk, M.H., Brett, M., Haldane, A., del Río, J.F., Wiebe, M., Peterson, P., Gérard-Marchant, P., Sheppard, K., Reddy, T., Weckesser, W., Abbasi, H., Gohlke, C., Oliphant, T.E., 2020. Array programming with NumPy. Nature 585, 357–362. URL: https://www.nature.com/articles/s41586-020-2649-2, doi:10.1038/s41586-020-2649-2.

Hawthorne, J.C., Ampuero, J.P., 2017. A phase coherence approach to identifying co-located earthquakes and tremor. Geophysical Journal International , ggx012URL: https://academic.oup.com/gji/article-lookup/doi/10.1093/gji/ggx012, doi:10.1093/gji/ggx012.

Helmstetter, A., Sornette, D., 2003a. Båth's law derived from the Gutenberg-Richter law and from aftershock properties. Geophysical Research Letters 30, 2003GL018186. URL: https://onlinelibrary.wiley.com/doi/abs/10.1029/2003GL018186, doi:10.1029/2003GL018186.

Helmstetter, A., Sornette, D., 2003b. Foreshocks explained by cascades of triggered seismicity. Journal of Geophysical Research: Solid Earth 108. URL: http://doi.wiley.com/10.1029/2003JB002409, doi:10.1029/2003JB002409.

Helmstetter, A., Sornette, D., 2003c. Importance of direct and indirect triggered seismicity in the ETAS model of seismicity. Geophysical Research Letters 30. URL: https://onlinelibrary.wiley.com/doi/abs/10.1029/2003GL017670, doi:10.1029/2003GL017670. _eprint: https://onlinelibrary.wiley.com/doi/pdf/10.1029/2003GL017670 tex.ids= helmstetter2003a.

Helmstetter, A., Sornette, D., Grasso, J.R., 2003. Mainshocks are aftershocks of conditional foreshocks: How do foreshock statistical properties emerge from aftershock laws. Journal of Geophysical Research: Solid Earth 108. URL: http://doi.wiley.com/10.1029/2002JB001991, doi:10.1029/2002JB001991. publisher: John Wiley & Sons, Ltd.

Hosseini, K., Sigloch, K., 2017. ObspyDMT: a Python toolbox for retrieving and processing large seismological data sets. Solid Earth 8, 1047–1070. URL: https://www.solid-earth.net/8/1047/2017/, doi:10.5194/se-8-1047-2017.

Hunter, J.D., 2007. Matplotlib: A 2D Graphics Environment. Computing in Science & Engineering 9, 90–95. URL: http://ieeexplore.ieee.org/document/4160265/, doi:10.1109/MCSE.2007.55.

Johnson, P.A., Ferdowsi, B., Kaproth, B.M., Scuderi, M., Griffa, M., Carmeliet, J., Guyer, R.A., Le Bas, P.Y., Trugman, D.T., Marone, C., 2013. Acoustic emission and microslip precursors to stick-slip failure in sheared granular material. Geophysical Research Letters 40, 5627–5631. URL: https://onlinelibrary.wiley.com/doi/abs/10.1002/2013GL057848, doi:10.1002/2013GL057848. _eprint: https://onlinelibrary.wiley.com/doi/pdf/10.1002/2013GL057848.

Jones, L., Molnar, P., 1976. Frequency of foreshocks. Nature 262, 677–679. URL: https://www.nature.com/articles/262677a0, doi:10.1038/262677a0. number: 5570 Publisher: Nature Publishing Group.

Kato, A., Fukuda, J., Nakagawa, S., Obara, K., 2016. Foreshock migration preceding the 2016 Mw 7.0 Kumamoto earthquake, Japan. Geophysical Research Letters 43, 8945–8953. URL: https://onlinelibrary.wiley.com/doi/abs/10.1002/2016GL070079, doi:10.1002/2016GL070079. _eprint: https://onlinelibrary.wiley.com/doi/pdf/10.1002/2016GL070079.

Keilis-Borok, V.I., 1957. The determination of earthquake mechanism, using both longitudinal and traverse waves. Annals of Geophysics 10, 18. URL: http://www.annalsofgeophysics.eu/index.php/annals/article/view/5882, doi:10.4401/ag-5882.

Kennett, B.L.N., Engdahl, E.R., Buland, R., 1995. Constraints on seismic velocities in the Earth from traveltimes. Geophysical Journal International 122, 108–124. URL: https://academic.oup.com/gji/article-lookup/doi/10.1111/j.1365-246X.1995.tb03540.x, doi:10.1111/j.1365-246X.1995.tb03540.x.

Latour, S., Schubnel, A., Nielsen, S., Madariaga, R., Vinciguerra, S., 2013. Characterization of nucleation during laboratory earthquakes. Geophysical Research Letters 40, 5064–5069. URL: https://onlinelibrary.wiley.com/doi/abs/10.1002/grl.50974, doi:10.1002/grl.50974. _eprint: https://onlinelibrary.wiley.com/doi/pdf/10.1002/grl.50974 tex.ids= Latour2013.

Lengliné, O., Enescu, B., Peng, Z., Shiomi, K., 2012. Decay and expansion of the early aftershock activity following the 2011, M $_W$ 9.0 Tohoku earthquake. Geophysical Research Letters 39. URL: http://doi.wiley.com/10.1029/2012GL052797, doi:10.1029/2012GL052797.

Liu, Y., Rice, J.R., 2007. Spontaneous and triggered aseismic deformation transients in a subduction fault model. Journal of Geophysical Research: Solid Earth 112, 1–23. doi:10.1029/2007JB004930.

Marone, C., 1998. Laboratory-Derived Friction Laws and Their Application to Seismic Faulting. Annual Review of Earth and Planetary Sciences 26, 643–696. URL: https://doi.org/10.1146/annurev.earth.26.1.643, doi:10.1146/annurev.earth.26.1.643. _eprint: https://doi.org/10.1146/annurev.earth.26.1.643.

McGuire, J., Boettcher, M., Jordan, T., 2005. Foreshock sequences and short-term earthquake predictability on East Pacific Rise transform faults. Nature 434, 457–61. doi:10.1038/nature03377.

McLaskey, G.C., Kilgore, B.D., 2013. Foreshocks during the nucleation of stick-slip instability. Journal of Geophysical Research: Solid Earth 118, 2982–2997. URL: http://doi.wiley.com/10.1002/jgrb.50232, doi:10.1002/jgrb.50232. tex.ids= mclaskey2013.

McLaskey, G.C., Lockner, D.A., 2014. Preslip and cascade processes initiating laboratory stick slip. Journal of Geophysical Research: Solid Earth 119, 6323–6336. URL: https://onlinelibrary.wiley.com/doi/abs/10.1002/2014JB011220, doi:10.1002/2014JB011220. _eprint: https://onlinelibrary.wiley.com/doi/pdf/10.1002/2014JB011220.

Naif, S., Key, K., 2018. Hikurangi Trench Regional Electromagnetic Survey to Image the Subduction Thrust.

Ogata, Y., 1988. Statistical Models for Earthquake Occurrences and Residual Analysis for Point Processes. Journal of the American Statistical Association 83, 9–27. URL: https://www.jstor.org/stable/2288914, doi:10.2307/2288914. publisher: [American Statistical Association, Taylor & Francis, Ltd.].

Ohnaka, M., 2000. A Physical Scaling Relation Between the Size of an Earthquake and its Nucleation Zone Size. Pure and Applied Geophysics 157, 2259–2282. URL: http://link.springer.com/10.1007/PL00001084, doi:10.1007/PL00001084.

Parsons, T., 2002. Global Omori law decay of triggered earthquakes: Large aftershocks outside the classical aftershock zone. Journal of Geophysical Research: Solid Earth 107, ESE 9–1–ESE 9–20. URL: http://doi.wiley.com/10.1029/2001JB000646, doi:10.1029/2001JB000646.

Peng, Z., Vidale, J.E., Ishii, M., Helmstetter, A., 2007. Seismicity rate immediately before and after main shock rupture from high-frequency waveforms in Japan. Journal of Geophysical Research 112, B03306. URL: http://doi.wiley.com/10.1029/2006JB004386, doi:10.1029/2006JB004386.

Richards-Dinger, K., Stein, R.S., Toda, S., 2010. Decay of aftershock density with distance does not indicate triggering by dynamic stress. Nature 467, 583–586. doi:10.1038/nature09402. publisher: Nature Publishing Group.

Ross, G.J., 2021. Bayesian Estimation of the ETAS Model for Earthquake Occurrences. Bulletin of the Seismological Society of America 111, 1473–1480.

URL: https://pubs.geoscienceworld.org/ssa/bssa/article/111/3/1473/597788/Bayesian-Estimation-of-the-ETAS-Model-for, doi:10.1785/0120200198.

Rouet-Leduc, B., Hulbert, C., Lubbers, N., Barros, K., Humphreys, C.J., Johnson, P.A., 2017. Machine Learning Predicts Laboratory Earthquakes. Geophysical Research Letters 44, 9276–9282. URL: https://onlinelibrary.wiley.com/doi/abs/10.1002/2017GL074677, doi:10.1002/2017GL074677. _eprint: https://onlinelibrary.wiley.com/doi/pdf/10.1002/2017GL074677.

Rubin, A.M., Ampuero, J.P., 2005. Earthquake nucleation on (aging) rate and state faults. Journal of Geophysical Research: Solid Earth 110. URL: http://doi.wiley.com/10.1029/2005JB003686, doi:10.1029/2005JB003686.

Scholz, C.H., 1968. The frequency-magnitude relation of microfracturing in rock and its relation to earthquakes. Bulletin of the Seismological Society of America 58, 399–415. URL: https://doi.org/10.1785/BSSA0580010399, doi:10.1785/BSSA0580010399.

Seif, S., Zechar, J.D., Mignan, A., Nandan, S., Wiemer, S., 2018. Foreshocks and Their Potential Deviation from General Seismicity. Bulletin of the Seismological Society of America 109, 1–18. URL: https://doi.org/10.1785/0120170188, doi:10.1785/0120170188.

Shearer, P.M., 2012. Self-similar earthquake triggering, Båth's law, and foreshock/aftershock magnitudes: Simulations, theory, and results for southern California. Journal of Geophysical Research: Solid Earth 117, 1–15. doi:10.1029/2011JB008957.

Tape, C., Holtkamp, S., Silwal, V., Hawthorne, J.C., Kaneko, Y., Ampuero, J.P., Ji, C., Ruppert, N., Smith, K., West, M.E., 2018. Earthquake nucleation and fault slip complexity in the lower crust of central Alaska. Nature Geoscience 11, 536–541. doi:10.1038/s41561-018-0144-2.

Trugman, D.T., Ross, Z.E., 2019. Pervasive Foreshock Activity Across Southern California. Geophysical Research Letters 46, 8772–8781. URL: https://onlinelibrary.wiley.com/doi/10.1029/2019GL083725, doi:10.1029/2019GL083725. tex.ids= Trugman2019, trugman2019c.

Utsu, T., Ogata, Y., S, R., Matsu'ura, 1995. The Centenary of the Omori Formula for a Decay Law of Aftershock Activity. Journal of Physics of the Earth 43, 1–33. URL: http://joi.jlc.jst.go.jp/JST.Journalarchive/jpe1952/43.1?from=CrossRef, doi:10.4294/jpe1952.43.1.

Virtanen, P., Gommers, R., Oliphant, T.E., Haberland, M., Reddy, T., Cournapeau, D., Burovski, E., Peterson, P., Weckesser, W., Bright, J., van der Walt, S.J., Brett, M., Wilson, J., Millman, K.J., Mayorov, N., Nelson, A.R.J., Jones, E., Kern, R., Larson, E., Carey, C.J., Polat, \., Feng, Y., Moore, E.W., VanderPlas, J., Laxalde, D., Perktold, J., Cimrman, R., Henriksen, I., Quintero, E.A., Harris, C.R., Archibald, A.M., Ribeiro, A.H., Pedregosa, F., van Mulbregt, P., SciPy 1.0 Contributors, Vijaykumar, A., Bardelli, A.P., Rothberg, A., Hilboll, A., Kloeckner, A., Scopatz, A., Lee, A., Rokem, A., Woods, C.N., Fulton, C., Masson, C., Häggström, C., Fitzgerald, C., Nicholson, D.A., Hagen, D.R., Pasechnik, D.V., Olivetti, E., Martin, E., Wieser, E., Silva, F., Lenders, F., Wilhelm, F., Young, G., Price, G.A., Ingold, G.L., Allen, G.E., Lee, G.R., Audren, H., Probst, I., Dietrich, J.P., Silterra, J., Webber, J.T., Slavič, J., Nothman, J., Buchner, J., Kulick, J., Schönberger, J.L., de Miranda Cardoso, J.V., Reimer, J., Harrington, J., Rodríguez, J.L.C., Nunez-Iglesias, J., Kuczynski, J., Tritz, K., Thoma, M., Newville, M., Kümmerer, M., Bolingbroke, M., Tartre, M., Pak, M., Smith, N.J., Nowaczyk, N., Shebanov, N., Pavlyk, O., Brodtkorb, P.A., Lee, P., McGibbon, R.T., Feldbauer, R., Lewis, S., Tygier, S., Sievert, S., Vigna, S., Peterson, S., More, S., Pudlik, T., Oshima, T., Pingel, T.J., Robitaille, T.P., Spura, T., Jones, T.R., Cera, T., Leslie, T., Zito, T., Krauss, T., Upadhyay, U., Halchenko, Y.O., Vázquez-Baeza, Y., 2020. SciPy 1.0: fundamental algorithms for scientific computing in Python. Nature Methods 17, 261–272. URL: http://www.nature.com/articles/s41592-019-0686-2, doi:10.1038/s41592-019-0686-2.

Wallace, L.M., Barnes, P., Beavan, J., Van Dissen, R., Litchfield, N., Mountjoy, J., Langridge, R., Lamarche, G., Pondard, N., 2012. The kinematics of a transition from subduction to strike-slip: An example from the central New Zealand plate boundary. Journal of Geophysical Research: Solid Earth 117. doi:10.1029/2011JB008640.

Withers, M., Aster, R., Young, C., Beiriger, J., Harris, M., Moore, S., Trujillo, J., 1998. A comparison of select trigger algorithms for automated global seismic phase and event detection. Bulletin of the Seismological Society of America 88, 95–106. Tex.ids= withers1998.

Yamanaka, Y., Shimazaki, K., 1990. Scaling relationship between the number of aftershocks and the size of the main shock. Journal of Physics of the Earth 38, 305–324. URL: http://www.jstage.jst.go.jp/article/jpe1952/38/4/38_4_305/_article, doi:10.4294/jpe1952.38.305.

Yoon, C.E., Yoshimitsu, N., Ellsworth, W.L., Beroza, G.C., 2019. Foreshocks and Mainshock Nucleation of the 1999 Mw 7.1 Hector Mine, California, Earthquake. Journal of Geophysical Research: Solid Earth 124, 1569–1582. URL: https://onlinelibrary.wiley.com/doi/abs/10.1029/2018JB016383, doi:10.1029/2018JB016383. _eprint: https://onlinelibrary.wiley.com/doi/pdf/10.1029/2018JB016383.